FISEVIER

Contents lists available at ScienceDirect

Earth and Planetary Science Letters

www.elsevier.com/locate/epsl



Heterodynes dominate precipitation isotopes in the East Asian monsoon region, reflecting interaction of multiple climate factors



Elizabeth K. Thomas ^{a,*,1}, Steven C. Clemens ^a, Youbin Sun ^b, Warren L. Prell ^a, Yongsong Huang ^a, Li Gao ^a, Shannon Loomis ^c, Guangshan Chen ^d, Zhengyu Liu ^d

- ^a Department of Earth, Environmental, and Planetary Sciences, Brown University, Providence, RI 02912, USA
- b State Key Laboratory of Loess and Quaternary Geology, Chinese Academy of Sciences, Xi'an, 710061, China
- ^c Jackson School of Geosciences, The University of Texas at Austin, Austin, TX, USA
- ^d Department of Atmospheric and Ocean Sciences, University of Wisconsin–Madison, Madison, WI, USA

ARTICLE INFO

Article history: Received 24 June 2016 Received in revised form 22 September 2016

Accepted 25 September 2016 Available online 10 October 2016 Editor: H. Stoll

Keywords: monsoon leaf wax hydrogen isotope hydroclimate loess molecular paleoclimate isotope hydrology

ABSTRACT

For the past decade, East Asian monsoon history has been interpreted in the context of an exceptionally well-dated, high-resolution composite record of speleothem oxygen isotopes ($\delta^{18}O_{cave}$) from the Yangtze River Valley. This record is characterized by a unique spectral response, with variance concentrated predominantly within the precession band and an enigmatic lack of variance at the eccentricity and obliquity bands. Here we examine the spectral characteristics of all existing >250-kyr-long terrestrial water isotope records in Asia, including a new water isotope record using leaf wax hydrogen isotope ratios from the Chinese Loess Plateau. There exist profound differences in spectral characteristics among all orbital-scale Asian water isotope records. We demonstrate that these differences result from latitudinal gradients in the influence of the winter and summer monsoons, both of which impact climate and water isotopes throughout East Asia. Water isotope records therefore do not reflect precipitation during a single season or from a single circulation system. Rather, water isotope records in East Asia reflect the complex interplay of oceanic and continental moisture sources, operating at multiple Earth-orbital periods. These non-linear interactions are reflected in water isotope spectra by the presence of heterodynes. Although complex, we submit that water isotope records, when paired with rapidly developing isotope-enabled model simulations, will have the potential to elucidate mechanisms causing seasonal precipitation variability and moisture source variability in East Asia.

© 2016 Elsevier B.V. All rights reserved.

1. Introduction

1.1. Motivation

For the past decade, well-dated, high-resolution records of speleothem oxygen isotopes ($\delta^{18} O_{cave}$) from the Yangtze River Valley have been used as the basis for inferring East Asian monsoon history (Cheng et al., 2016, 2009; Wang et al., 2008). The composite of these records is characterized by a unique spectral response, with variance concentrated predominantly within the precession band, and an enigmatic lack of variance at the eccentricity and obliquity bands. Yet, orbital-scale records of East Asian monsoon strength not based on water isotope proxies contain spectral vari

ance at all three of the primary orbital periods, suggesting that the monsoon is influenced by mechanisms operating at all three of the primary orbital bands (Clemens et al., 2010; Sun et al., 2015, 2010). Despite these differences between proxy records, the $\delta^{18}O_{cave}$ record has been interpreted to reflect summer rainfall as a direct function of East Asian summer monsoon circulation strength (Cheng et al., 2016, 2009; Wang et al., 2008). In turn, the summer monsoon has been interpreted to respond solely to the precession-band forcing of Northern Hemisphere summer insolation. Other research suggests, however, that precipitation isotopes (δ^{18} O and δ^{2} H) in East Asia are more complex, and likely also reflect isotopic distillation along the pathway from the Indian Monsoon or other moisture source regions (Lee et al., 2012; LeGrande and Schmidt, 2009; Liu et al., 2014; Pausata et al., 2011), and/or a mix of precipitation isotope variability from multiple moisture sources and seasons (Baker et al., 2015; Caley et al., 2014; Clemens et al., 2010; Duan et al., 2016; Maher, 2008; Thomas et al., 2014a). This broad array of interpretations reflects the complexities of precipitation isotopes, which change as a func-

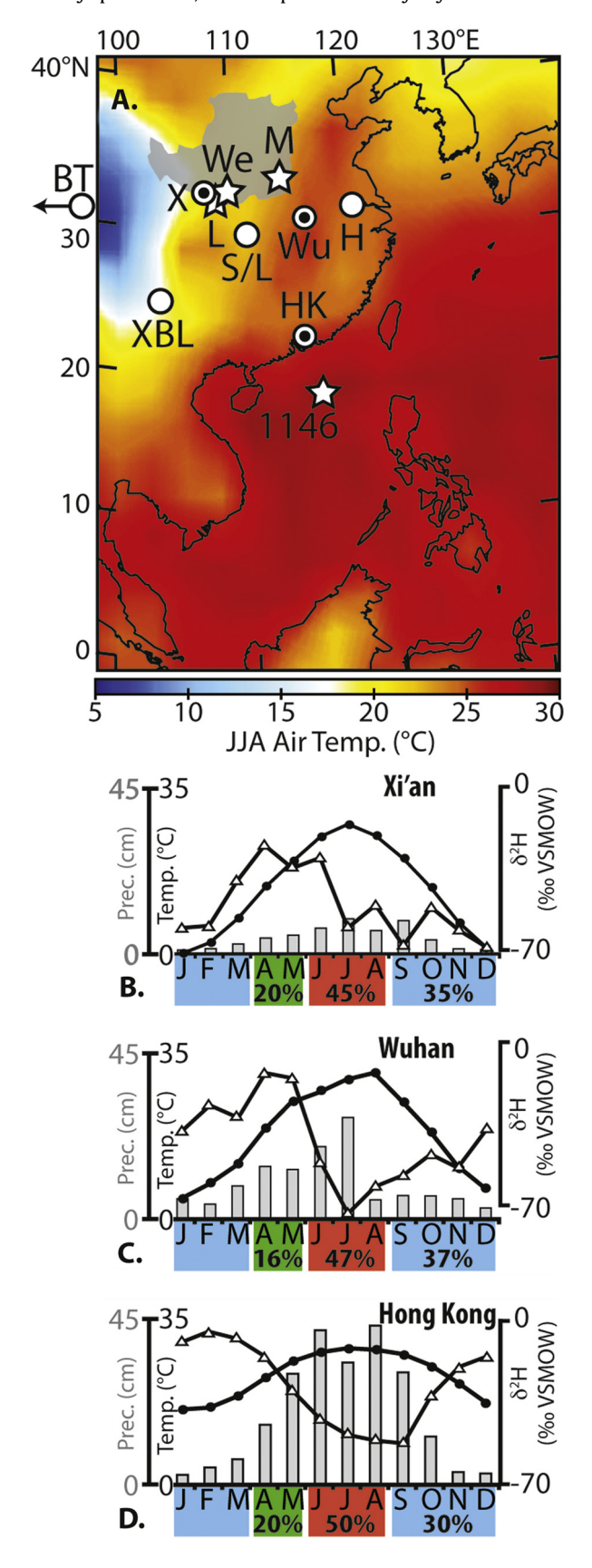
^{*} Corresponding author.

E-mail address; ekthomas@buffalo.edu (E.K. Thomas).

¹ Current address: Department of Geology, University at Buffalo, Buffalo, NY 14260, USA.

tion of moisture source area, seasonality, temperature, and aridity, among other variables (Bradley et al., 2010; Duan et al., 2016; Orland et al., 2015; Thomas et al., 2016).

Multiple environmental variables operating at different seasons are not consistent with a simple spectral response dominated by precession, driven predominantly by northern hemi-



sphere insolation forcing. Instead, such a system should be characterized by complex spectra, reflecting interaction among these multiple environmental variables (Clemens et al., 2010; Rial and Anaclerio, 2000). Understanding the influence of environmental variables on precipitation isotopes is key to our ability to effectively use precipitation isotope records as indicators of past climate change. Five >250-kyr-long water-isotope records exist for the Asian monsoon region (Fig. 1), all exhibiting profoundly different spectral responses (Cai et al., 2015; Kathayat et al., 2016; Thomas et al., 2014a; Wang et al., 2008). Each of these records has heterodyne-rich spectra, implying that multiple environmental forcing mechanisms influence each of these records.

1.2. Modern precipitation sources and seasonality

Modern gradients in temperature, precipitation seasonality and moisture source regions across East Asia cause gradients in precipitation isotopes (Fig. 1) (Baker et al., 2015; Clemens et al., 2010; IAEA/WMO, 2011; Johnson and Ingram, 2004; Sun and Wang, 2014). In the Pearl River Valley, southeastern China, precipitation is derived from the Bay of Bengal, the South China Sea, the western Pacific, and from locally recycled moisture (Sun and Wang, 2014). Precipitation isotopes in southeastern China are ²H-enriched during the winter, when moisture is derived mainly from locally recycled sources, and is ²H-depleted during the summer, when moisture is derived from far-traveled sources (Fig. 1D) (IAEA/WMO, 2011). In the Yangtze River Valley, central China, precipitation is derived from similar sources as in southeastern China, but with a greater contribution year-round from northwesterly and locallyrecycled moisture sources (Sun and Wang, 2014). Precipitation isotopes in central China are most ²H-enriched during the spring, when oceanic moisture is derived mainly from the East China Sea (Chiang et al., 2015; Clemens et al., 2010), and otherwise exhibit similar patterns as in southeastern China (Fig. 1C). On the Chinese Loess Plateau, northern China, precipitation is derived mainly from locally recycled moisture, but is also derived from the Bay of Bengal, the South China Sea, the western Pacific, and from northwesterly sources. Oceanic moisture sources are reduced during the winter. Precipitation isotopes in Xi'an, northern China exhibit similar patterns as in central China (Fig. 1B). Modern precipitation patterns suggest that the winter monsoon (continental moisture) exerts a greater influence in northern East Asia, whereas the summer monsoon influences all of East Asia (Baker et al., 2015; Sun and Wang, 2014). Precipitation moisture source and transport dynamics likely changed over geological time scales, influencing precipitation isotopes differently in each region (Baker et al., 2015; Chiang et al., 2015). Water isotope proxy records reflect changes in moisture sources and seasonality and can elucidate regional variations in mechanisms that influence precipitation isotopes.

1.3. Orbital-scale water isotope records

Orbital-scale terrestrial water isotope records in East Asia are derived from leaf wax hydrogen isotope ratios ($\delta^2 H_{wax}$) and speleothem carbonate oxygen isotope ratios ($\delta^{18} O_{cave}$). Existing

Fig. 1. Location of study sites and modern climatology. A. Map of East Asia showing study sites on the Chinese Loess Plateau (stars: L—Lantian, We—Weinan, M—Mangshan), the Yangtze River Valley and other cave sites (white dots: BT—Bittoo cave, XBL—Xiaobailong cave, S/L—Sanbao and Linzhu caves, H—Hulu cave), and the South China Sea (star: ODP Site 1146, which receives terrestrial material from the Pearl River catchment in southeastern China) (Thomas et al., 2014a). Location of modern meteorological stations shown with bullseyes (X—Xi'an, Wu—Wuhan, HK—Hong Kong). B.–D. Data from modern meteorological stations showing monthly mean precipitation (Prec., gray bars; seasonal percent of annual precipitation is at bottom), air temperature (black), and precipitation δ^2 H (δ^2 H_p, white) (IAEA/WMO, 2011). VSMOW—Vienna standard mean ocean water. B. Xi'an. C. Wuhan. D. Hong Kong.

East Asian records span a latitudinal gradient from the Pearl River Valley in southeastern China to the Yangtze River Valley in central China (Fig. 1) (Thomas et al., 2014a; Wang et al., 2008). There are additional orbital-scale $\delta^{18}{\rm O}_{\rm cave}$ records from southwestern China and the southeastern Himalaya (Cai et al., 2015; Kathayat et al., 2016).

Here we expand the spatial coverage of orbital-scale water isotope variability in East Asia northward by generating a 360-kyrlong $\delta^2 H_{\text{wax}}$ record on the Chinese Loess Plateau in continental East Asia. We compare spectra of all these records to test the hypothesis that on orbital timescales, summer monsoon dynamics influence all regions of East Asia, and the winter monsoon influences precipitation isotopes in northern China more than in southern China.

2. Study site

The Chinese Loess Plateau at 34° to 42°N in East Asia (Fig. 1) contains alternating loess and paleosol sequences spanning multiple glacial cycles. We report a continuous 360-kyr-long record of $\delta^2 H_{\text{wax}}$ from Weinan (34.42°N, 109.60°E; 680 m above sea level) and Lantian (34,20°N, 109,20°E; 620 m above sea level) (Gao et al., 2012a) on the southeastern Chinese Loess Plateau, along with air temperature reconstructed at Weinan and Mangshan (34.94°N, 113.37°E), and grain size, and magnetic susceptibility at Weinan (Fig. 2). This is the warmest and wettest portion of the loess plateau, conducive to high in situ plant productivity. The modern growing season on the southeastern loess plateau is April through September (Chen et al., 2005). Modern annual precipitation at Xi'an, 60 km southwest of Weinan, is 570 mm, with ca. 80% falling during the growing season (Fig. 1) (NCDC NOAA, 2012). Average annual, summer, and winter temperature are 13.5 °C, 25.5 °C, and 1.3 °C, respectively (IAEA/WMO, 2011).

3. Methods and approach

3.1. Chinese Loess Plateau leaf wax $\delta^2 H$ as a proxy for precipitation $\delta^2 H$

Plants produce long-chain n-alkyl lipids, or leaf waxes, as part of the epicuticular wax coating on their leaves, which provides protection against evaporation and physical and microbial damage (Kahmen et al., 2013). $\delta^2 H$ of leaf waxes from modern sediments in Eastern China is correlated with source water $\delta^2 H$, offset by a biosynthetic fractionation that is largely constant for specific compounds (Rao et al., 2009). Precipitation $\delta^2 H$ changes as a function of ice volume, moisture source, condensation temperature, and aridity (Johnson and Ingram, 2004; Lee et al., 2012). Moreover, seasonality of leaf wax production and aridity effects on plants can cause changes in $\delta^2 H_{\text{wax}}$ (Kahmen et al., 2013). We discuss in detail how these variables influence precipitation $\delta^2 H$ and $\delta^2 H_{\text{wax}}$ in the Appendix (Gao et al., 2012b; Liu and Huang, 2005).

 $\delta^2 H_{wax}$ on the Chinese Loess Plateau reflects a combination of variables, including moisture source and seasonality, temperature, and aridity. Records of precipitation isotopes elsewhere in East Asia also reflect these multiple variables (Baker et al., 2015; Clemens et al., 2010; Duan et al., 2016; Thomas et al., 2016, 2014a). The relative importance of each variable depends on the location, as variability of precipitation sources, seasonality, temperature, ice volume, and aridity differ in space and time.

3.2. Sample collection and proxy analysis

2,050 sediment samples were collected at 2.5 cm resolution from trenches dug into the floor of a brick pit and the sides of a steep-walled valley at Weinan. All of these samples were analyzed for grain size and magnetic susceptibility. Prior to grain size

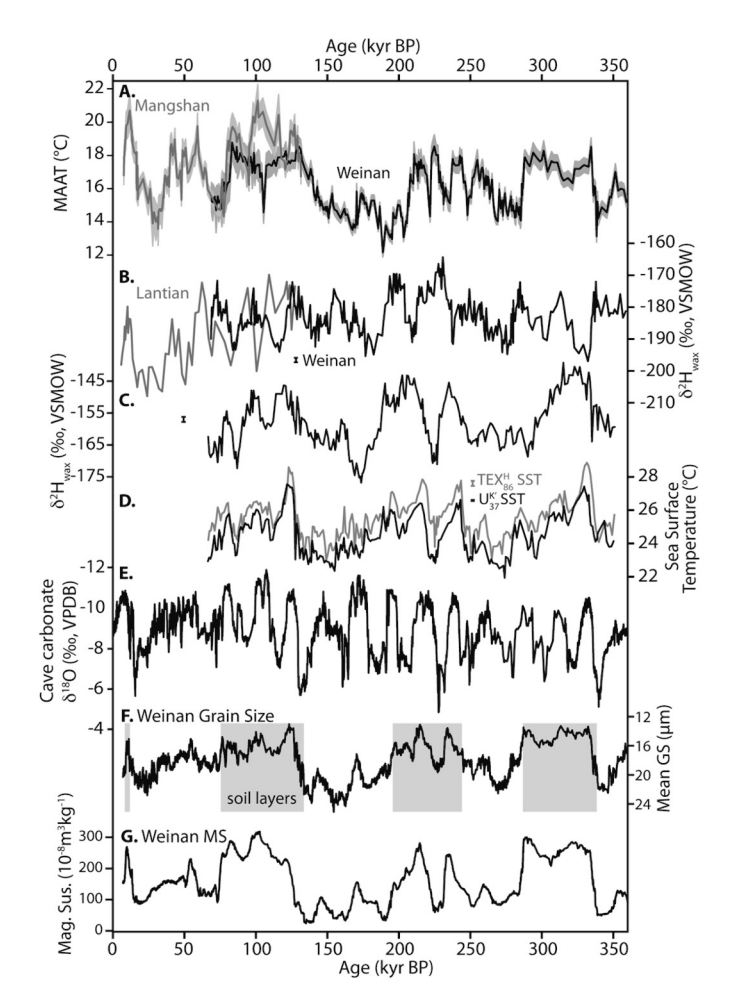


Fig. 2. Time series of temperature, water isotopes, summer monsoon strength, and winter monsoon strength in East Asia during the past 360 kyr. A. Chinese Loess Plateau brGDGT-inferred MAAT at Mangshan (gray) and Weinan (black), gray shading is 1σ bootstrapped calibration error. B. Chinese Loess Plateau $\delta^2 H_{wax}$ at Lantian (gray) and Weinan (black). Vertical bars on panels B, C, and D show pooled standard deviation (SD), 1.6‰ for loess $\delta^2 H_{wax}$. Y axes of $\delta^2 H_{wax}$ records are oriented for comparison with temperature. VSMOW–Vienna standard mean ocean water. C. ODP Site $1146\delta^2 H_{wax}$ (SD = 1.6%) (Thomas et al., 2014a). D. ODP Site 1146 SST (U_{37}^{*}): black, SD = 0.07° C; TEX $_{86}^{H}$: gray, SD = 0.3° C) (Thomas et al., 2014a). E. Yangtze River Valley $\delta^{18}O_{cave}$ from Hulu, Sanbao, and Linzhu caves, China (Caballero-Gill et al., 2012; Cheng et al., 2009; Wang et al., 2008). VPDB–Vienna Peedee belemnite. F. Mean grain size at Weinan on the Chinese Loess Plateau with soil stratigraphy highlighted in gray. G. Magnetic susceptibility at Weinan on the Chinese Loess Plateau.

measurements, all samples were pretreated by removal of organic matter and carbonate using $\rm H_2O_2$ and HCl, respectively, and then dispersed by ultrasonication with 10 ml 10% (NaPO_3)_6 solution. The grain size distribution was determined using a Malvern 2000 laser instrument. Replicate analyses indicate that the mean grain size has an analytical error of <2%. Magnetic susceptibility was measured with a Bartington MS 2 meter.

At Weinan, 310 sediment samples were collected at 5 to 10 cm resolution, and at Lantian 35 samples were collected at 5 to 20 cm resolution for organic analysis. These sites are in the warm, wet portion of the Chinese Loess Plateau, conducive to high *in situ* production of leaf wax fatty acids and branched GDGTs. *In situ* production for the vast majority of samples at Weinan overwhelms detrital inputs of branched GDGTs and C_{28} n-alkanoic acids (Appendix A2). Free lipids were extracted from freeze-dried samples (ca. 130 g dry weight) with an Accelerated Solvent Extractor 200 (Dionex) using dichloromethane (DCM):methanol 19:1 (v:v). A known amount of $C_{20:1}$ alkenoic acid and synthetic C_{46} GDGT

(Huguet et al., 2006) were added as internal standards to each extract before separation. The extracts were dried under N₂ and separated on aminopropyl silica gel flash columns, eluting neutral fractions with DCM:methanol 1:1 (v:v) and acid fractions with 4% acetic acid in diethyl ether. All flash column separations used three column volumes of each eluent. Acid fractions were methylated in anhydrous 5% HCl in methanol at 60 °C overnight. Samples were further cleaned using silica gel flash columns: apolar compounds were removed with hexane, fatty acid methyl esters (FAMEs, our target compounds) were eluted with DCM. Neutral fractions were separated on aluminum oxide flash columns, eluting apolar fractions with hexane:DCM 9:1 (v:v), ketone fractions with hexane:DCM 1:1 (v:v; four column volumes), and polar fractions with DCM:methanol 1:1 (v:v). Polar fractions were dissolved in hexane:isopropanol 99:1 (v:v), and filtered through a 0.4 µm PTFE filter.

Branched GDGTs were analyzed using high performance liquid chromatography–mass spectrometry, using previously described methods (Peterse et al., 2014). An external standard was analyzed every 10 samples, and was continuously monitored to ensure minimal ($<0.5\,^{\circ}$ C) analytical drift. The pooled analytical error, calculated using replicate analyses of individual extracts (each sample was run 1 to 4 times), is 0.1 $^{\circ}$ C (1σ).

The hydrogen isotope ratio of the C_{28} FAME was determined using gas chromatography–pyrolysis–isotope ratio mass spectrometry at Brown University using previously described methods (Thomas et al., 2014a). Isotope values are expressed in per mille (‰) relative to Vienna Standard Mean Ocean Water (VSMOW). The pooled standard deviation for these analyses, calculated using the results of replicate analyses of each extract (each sample was run 2 to 4 times), is 1.6‰ (1 σ). Analysis of an external FAME standard consisting of C_{16} , C_{18} , C_{22} , C_{24} , and C_{26} FAMES, injected twice after every sixth sample injection, had an analytical error of 2‰ (1 σ). Measured FAME δ^2 H values were corrected for the isotopic contribution of the hydrogens added during methylation.

The carbon isotope ratio of the C_{28} fatty acid methyl ester (FAME) was determined using gas chromatography–combustion—isotope ratio mass spectrometry at Brown University using previously described methods (Thomas et al., 2014b). Isotope values are expressed in per mille (‰) relative to Vienna Pee Dee Belemnite (VPDB). The pooled standard deviation for these analyses, calculated using the results of replicate analyses of each extract, is 0.1‰ (1 σ). Analysis of an external FAME standard consisting of C_{16} , C_{18} , C_{22} , C_{24} , and C_{26} FAMES, injected once after every sixth sample injection (each sample was run 2 to 4 times), had an analytical error of <0.5‰ (1 σ). The measured FAME δ^{13} C values were corrected for the isotopic contribution of the carbon added during methylation.

3.3. Loess chronology

Winter winds carry dust from East Asian deserts east to the Chinese Loess Plateau. Larger grains are deposited near the desert source regions and smaller grains are deposited on the distal side of the loess plateau, causing a measurable grain size gradient on the Chinese Loess Plateau, from larger in the northwest to smaller in the southeast (Sun et al., 2006). At a given site on the Chinese Loess Plateau, grain size changes in response to wind strength, which is strongly coupled with changes in high latitude ice volume (Hao et al., 2012). Grain size has been used for decades to obtain chronological constraints for loess sequences on orbital time scales (Hao et al., 2012; Porter and An, 1995). The grain size age-model method has been verified by multiple independent dating methods, including optically stimulated luminescence, soil-loess profile stratigraphy, and magnetic reversal stratigraphy (Hao et al., 2012; Sun et al., 1998, 2012).

Weinan, Lantian, and Mangshan grain size was correlated to the radiometrically-constrained benthic foraminifera δ^{18} O record at ODP Site 1146 in the northern South China Sea (Fig. A1) (Caballero-Gill et al., 2012; Gao et al., 2012a; Sun et al., 2012). This yields a chronology independent of orbital tuning. The Lantian, Mangshan, and Weinan sections were spliced by correlating grain size between the sections. Lantian $\delta^2 H_{\text{wax}}$ and Mangshan MAAT data span 6 to 68 ka, and Weinan $\delta^2 H_{\text{wax}}$ and MAAT data span 69 to 360 ka. We use Lantian δ^{13} C data from Liu et al. (2005).

3.4. Temperature calibration

We use the modern soil dataset from semi-arid regions of China (Yang et al., 2014) and stepwise forward selection methods of Loomis et al. (2012) to convert GDGT fractional abundance to mean annual air temperature (MAAT). This modified calibration has similar RMSE (1.7 $^{\circ}$ C for Yang et al. (2014) and 1.6 $^{\circ}$ C for the modified calibration) and residual patterns as the Yang et al. (2014) calibration, but incorporates more of the GDGT compounds into the calculated temperature, which provides more structure in intervals where those added compounds exhibit variability (Fig. A2). The modified calibration equation is:

$$MAAT = 20.87 - 18.04^*IIIa + 38.88^*IIIb - 12.92^*IIa - 20.41^*IIb$$
$$- 30.27^*IIc + 12.94^*Ib$$

Based on the uppermost sample analyzed at Mangshan, this calibration overestimates modern mean annual temperature on the southeastern Chinese Loess Plateau by 3.5 to 4°C (Fig. A2). The uppermost sample analyzed at Mangshan may not be modern, as there is widespread anthropogenic disturbance of uppermost sections on the Chinese Loess Plateau, and there is evidence for anthropogenic disturbance at this site (Peterse et al., 2014). The lack of a modern sample in our dataset may explain the mismatch between modern instrumental temperature and the uppermost proxy-inferred MAAT. Additionally, although bacteria are active year-round, they may be more active during the warm, wet summer (Yang et al., 2014). Our analyses are based on the timing and amplitude, not the absolute value, of mid-latitude terrestrial air temperature changes. Thus, our conclusions do not change regardless of whether the GDGT proxy reconstructs mean annual air temperature or summer-biased mean annual air temperature.

3.5. Spectral analysis

The Arand software package (Howell et al., 2006) was used to calculate power spectra, coherency, and phase of time series. Arand explicitly accounts for discontinuous data, which are present in the Bittoo and Xiaobailong cave records (Cai et al., 2015; Kathayat et al., 2016).

ETP was calculated by normalizing and averaging the three orbital parameters eccentricity, obliquity (tilt), and precession (minimum precession defined as June 21 perihelion) (Laskar et al., 2004). Analyseries was used to conduct f-tests of spectral peak significance (Paillard et al., 1996).

3.6. Long transient general circulation model experiment

Simulations were conducted with the Community Climate System Model, version 3 (CCSM3), following methods and boundary detailed in Chen et al. (2011). The resolution used was a T31 atmosphere–land horizontal grid (equivalent to a 3.75° latitude/longitude grid) with 26 levels in the atmosphere, and an ocean–sea ice horizontal grid of 100×116 points with 25 levels in the ocean extending to 5 km depth.

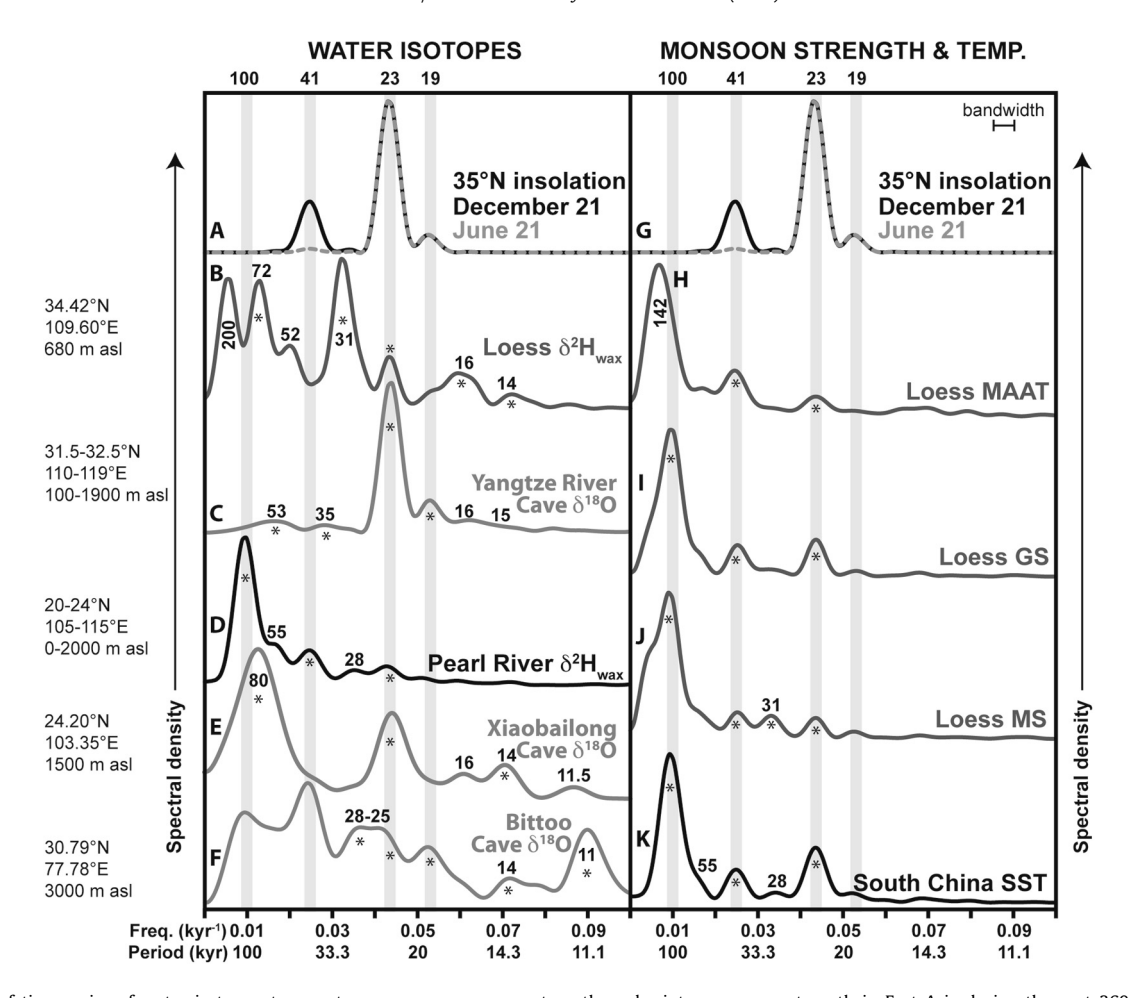


Fig. 3. Spectra of time series of water isotopes, temperature, summer monsoon strength, and winter monsoon strength in East Asia during the past 360 kyr. All spectral analyses span 8 to 360 ka, except the southern China sites, which span 67 to 350 ka, and the cave records, which span the length of the published records. Vertical bars highlight primary orbital periods, labeled with black numbers at top. Heterodyne peaks in individual records are labeled with black numbers. Asterisks indicate peaks that exceed the 80% confidence bound in an f-test for periods shorter than 1/3 the length of each record (Paillard et al., 1996). A. December 21 (solid black) and June 21 (dashed gray) insolation at 35°N (Laskar et al., 2004). B. Chinese Loess Plateau $\delta^2 H_{wax}$. C. Yangtze River Valley $\delta^{18} O_{cave}$ (Caballero-Gill et al., 2012; Cheng et al., 2009; Wang et al., 2008). D. Pearl River Valley $\delta^2 H_{wax}$ (Thomas et al., 2014a). E. Xiaobailong Cave $\delta^{18} O_{cave}$ (Cai et al., 2015). F. Bittoo Cave $\delta^{18} O_{cave}$ (Kathayat et al., 2016). G. Same as A. H. Chinese Loess Plateau brGDGT-inferred MAAT. I. Mean grain size at Weinan on the Chinese Loess Plateau. J. Magnetic susceptibility at Weinan on the Chinese Loess Plateau. K. South China Sea alkenone-inferred sea surface temperature (Thomas et al., 2014a).

We used a similar acceleration technique to those used in other paleoclimatic modeling studies (Lorenz and Lohmann, 2004). This technique enables us to gain insight into the temporal evolution of the climate system given restricted computer resources. Studies have shown that acceleration factors of 10 and 100 produced similar results (e.g., Lorenz and Lohmann, 2004). In our experiment, we chose 100 as the acceleration factor (the orbital forcing interval is 100 years). In this acceleration approach, the change in insolation forcing is quite small (less then 0.5 W/m²) from year to year at all latitudes in the shortest orbital cycle (precession).

The model was spun up for 200 model years at 300 ka, after which the transient simulations were run from 300 to 0 ka. At the end of each year of the simulation, the orbital parameters and the atmospheric greenhouse gases were advanced by 100 years. The experiment consisted of three separate simulations, beginning with an insolation only simulation, followed by addition of greenhouse gases, followed by addition of ice-volume and sea level. When the model boundary conditions changed (e.g., land-ocean boundaries changing due to sea level rise or fall equivalent to 40 m), all the components of the CCSM3 were reconfigured manually and the model was restarted using the previous year as the initial conditions. Successively adding boundary conditions is a reliable method for understanding the sensitivity of the model response to these forcing mechanisms. Model precipitation was averaged from the

four grid cells over the Chinese Loess Plateau (33 to $35^{\circ}N$, 108 to $110^{\circ}E$) and the Pearl River (20 to $25^{\circ}N$, 105 to $115^{\circ}E$).

4. Results

Between 6 and 360 ka, Chinese Loess Plateau $\delta^2 H_{wax}$ ranged from -165 to -210% (Fig. 2B). The loess $\delta^2 H_{wax}$ record has strong orbital-scale variability, but does not exhibit the classic saw-tooth structure of global ice volume (Fig. 2B, F) (Caballero-Gill et al., 2012). Moreover, the vast majority of spectral variance in loess $\delta^2 H_{wax}$ is at non-primary periods (e.g., 72, 31, 16, and 14 kyr; Fig. 3B). Chinese Loess Plateau $\delta^{13}C_{\text{wax}}$ ranged from -21 to -31%and contains similar spectral variance as $\delta^2 H_{wax}$, indicating $\delta^2 H_{wax}$ and $\delta^{13}C_{wax}$ are influenced by similar climate variables and/or that they influence each other on orbital time scales (Figs. A3A, A4). The spectral variance in loess $\delta^2 H_{wax}$ is in sharp contrast to $\delta^2 H_{wax}$ in the Pearl River Valley, which has variance at all three dominant orbital periods (100, 41, and 23 kyr; Fig. 3D) and $\delta^{18}O_{cave}$ in the Yangtze River Valley, which has dominant variance at precession periods (23 and 19 kyr; Fig. 3C). The fundamentally different time series and spectral characteristics between these three water isotope records indicates that either these proxies are biased differently because of the nature of the different speleothem and leaf wax archives, or the proxies reflect regional complexities of precipitation isotopes. Although the difference between $\delta^2 H_{\text{wax}}$ and $\delta^{18}O_{cave}$ may indicate differences in proxy biases, there are striking differences between the two $\delta^2 H_{wax}$ records themselves, indicating that there are, in fact, strong regional differences in precipitation isotopes (Fig. 3B, D). Equally striking differences between the $\delta^{18}O_{cave}$ spectra are evident (Fig. 3C, E, F), further implicating strong regional differences in precipitation isotopes, independent of proxy type. We hypothesize, therefore, that the changes in spectral variance along this latitudinal gradient are due to regional differences in climate and precipitation isotopes, specifically, a changing influence of summer and winter monsoon dynamics. We test this hypothesis using the following approach: (1) We determine the main environmental variables that influence water isotope variability on the Chinese Loess Plateau using multiple linear regression to combine independent records of temperature and summer and winter monsoon variability produced from the same section as $\delta^2 H_{\text{wax}}$, and (2) We use our understanding of the causes of variance in loess $\delta^2 H_{wax}$ to infer the causes of variance in other orbital-scale water isotope records in Asia and elucidate latitudinal changes in precipitation sources and seasonality.

5. Discussion

5.1. Determining the environmental variables that influence water isotope variability on the Chinese Loess Plateau

5.1.1. Chinese Loess Plateau $\delta^2 H_{wax}$ spectral variance is dominated by heterodynes

When compared with isotope records from the Pearl and Yangtze river valleys, the spectral variance of Chinese Loess Plateau $\delta^2 H_{\text{wax}}$ is unique, and dominated by non-primary periods at 72 and 31 kyr, with minor peaks at 23, 16, and 14 kyr (Fig. 3). The non-primary periods are heterodynes. Heterodynes result from the non-linear interaction of variables operating at primary orbital periods and can be calculated by adding or subtracting primary orbital frequencies (frequency = 1/period) (Clemens et al., 2010; Rial and Anaclerio, 2000). For example, the non-linear interaction of eccentricity and obliquity variance yields heterodynes at 28.7 and 72.6 kyr $(1/94.8 \pm 1/41.1 = 1/28.7$ and 1/72.6), consistent with the dominant periods observed in Chinese Loess Plateau $\delta^2 H_{\text{wax}}$ (Table 1). In order to determine the origin of the heterodynes in Chinese Loess Plateau $\delta^2 H_{wax}$, we must identify the various aspects of climate that influence precipitation δ^2H at primary orbital periods.

5.1.2. The Chinese Loess Plateau contains independent records of local temperature and summer and winter monsoons

The Chinese Loess Plateau is a unique and important archive because it contains independent orbital-scale records that reflect mean annual air temperature (branched glycerol dialkyl glycerol tetraethers, brGDGTs), summer monsoon strength (magnetic susceptibility, MS), and winter monsoon strength, which is strongly correlated with ice volume (grain size, GS) (Fig. 2A, F, G). Chinese Loess Plateau mean annual air temperature (MAAT), summer monsoon (MS), and winter monsoon (GS) all have dominant spectral variance at primary orbital periods (Fig. 3H–J) (Hao et al., 2012; Sun et al., 2015, 2012). MS contains minor variance at the 31 kyr heterodyne period (Fig. 3J). These spectra indicate that GS, MS, and brGDGTs have direct and relatively simple responses to single environmental variables (temperature, summer and winter monsoons), which vary at primary orbital periods. MS and GS have opposite phases at primary orbital periods (Table 2).

Temperature and the summer and winter monsoons are likely the main aspects of climate that influence precipitation and leaf wax δ^2 H on the Chinese Loess Plateau, either directly, or indirectly

Table 1 Heterodynes that result from Earth's primary orbital periods. Heterodynes that are similar to those found in Chinese Loess Plateau $\delta^2 H_{\text{wax}}$ are in bold italics. Heterodynes are calculated as follows: Period $1^{-1} \pm \text{Period } 2^{-1} = \pm \text{Heterodyne}^{-1}$.

| Period 1 | Period 2 | +Heterodyne | -Heterodyne | |
|----------|----------|-------------|-------------|--|
| 404.0 | 130.6 | 98.7 | | |
| 404.0 | 123.8 | 94.8 | 178.5 | |
| 404.0 | 98.7 | 79.3 | 130.6 | |
| 404.0 | 94.8 | 76.8 | 123.9 | |
| 404.0 | 53.9 | 47.6 | 62.2 | |
| 404.0 | 41.1 | 37.3 | 45.8 | |
| 404.0 | 23.7 | 22.4 | 25.2 | |
| 404.0 | 22.4 | 21.2 | 23.7 | |
| 404.0 | 19.3 | 18.4 | 20.3 | |
| 130.6 | 123.8 | 63.6 | 2377.7 | |
| 130.6 | 98.7 | 56.2 | 404.1 | |
| 130.6 | 94.8 | 54.9 | 345.8 | |
| 130.6 | 53.9 | 38.2 | 91.8 | |
| 130.6 | 41.1 | 31.3 | 60.0 | |
| 130.6 | 23.7 | 20.1 | 29.0 | |
| 130.6 | 22.4 | 19.1 | 27.0 | |
| 130.6 | 19.3 | 16.8 | 22.6 | |
| 123.8 | 98.7 | 54.9 | 486.8 | |
| 123.8 | 94.8 | 53.7 | 404.7 | |
| 123.8 | 53.9 | 37.6 | 95.5 | |
| 123.8 | 41.1 | 30.9 | 61.5 | |
| 123.8 | 23.7 | 19.9 | 29.3 | |
| 123.8 | 22.4 | 19.0 | 27.3 | |
| 123.8 | 19.3 | 16.7 | 22.9 | |
| 98.7 | 94.8 | 48.4 | 2399.2 | |
| 98.7 | 53.9 | 34.9 | 118.7 | |
| 98.7 | 41.1 | 29.0 | 70.4 | |
| 98.7 | 23.7 | 19.1 | 31.2 | |
| 98.7 | 22.4 | 18.3 | 29.0 | |
| 98.7 | 19.3 | 16.1 | 24.0 | |
| 94.8 | 53.9 | 34.4 | 124.9 | |
| 94.8 | 41.1 | 28.7 | 72.6 | |
| 94.8 | 23.7 | 19.0 | 31.6 | |
| 94.8 | 22.4 | 18.1 | 29.3 | |
| 94.8 | 19.3 | 16.0 | 24.2 | |
| 53.9 | 41.1 | 23.3 | 173.1 | |
| 53.9 | 23.7 | 16.5 | 42.3 | |
| 53.9 | 22.4 | 15.8 | 38.3 | |
| 53.9 | 19.3 | 14.2 | 30.1 | |
| 41.1 | 23.7 | 15.0 | 56.0 | |
| 41.1 | 22.4 | 14.5 | 49.2 | |
| 41.1 | 19.3 | 13.1 | 36.4 | |
| 23.7 | 22.4 | 11.5 | 408.4 | |
| 23.7 | 19.3 | 10.6 | 104.0 | |
| 22.4 | 19.3 | 10.4 | 139.5 | |

via the temperature or aridity effects on plant community composition. Correcting for the influence of each of these variables on $\delta^2 H_{\text{wax}}$ individually is dependent on assumptions that these corrections do not change through time (Thomas et al., 2014a). Instead, our approach is to use independent, locally-derived time series of temperature and summer and winter monsoons to test the degree to which these variables influence orbital-scale precipitation isotopes in northern China. This approach accounts for the effects of ice volume, temperature, and vegetation on $\delta^2 H_{\text{wax}}$, as these factors are all strongly influenced by one or more of the three time series (e.g., grain size is strongly correlated with ice volume (Hao et al., 2012), plant community on the Chinese Loess Plateau is influenced by temperature and rainfall (Liu et al., 2005), as recorded by MAAT and MS).

5.1.3. Summer and winter monsoon records combine to produce the heterodynes observed in Chinese Loess Plateau $\delta^2 H_{wax}$

We use multiple linear regression to combine our independent records of temperature and monsoon strength (MAAT, MS, and GS) to create a best-fit match of the Chinese Loess Plateau $\delta^2 H_{wax}$ record (Fig. 4). This model assumes that temperature and monsoon strength exert a linear influence on $\delta^2 H_{wax}$. While both MS

Table 2 Phase of proxy data relative to insolation forcing.

| Parameter | Precession phase (°) | Precession phase uncertainty (°) | Tilt phase (°) | Tilt phase uncertainty (°) | Eccentricity phase (°) | Eccentricity phase uncertainty (°) |
|--|----------------------------|---|----------------------|----------------------------------|------------------------------|---|
| Water isotopes | | | | | | |
| Chinese Loess Plateau δ ² H _{wax} ^a | -180 | 11 | | | | |
| Yangtze River Valley cave $\delta^{18}O^{a,b}$ | -60 | 3 | | | -89 | 20 |
| Pearl River Valley $\delta^2 H_{\text{wax}}^{\text{c,d}}$ | 51 | 10 | 70 | 14 | -174 | 7 |
| Chinese Loess Plateau δ ² H _{wax-T} ^a | | | 16 | 11 | | |
| Pearl River Valley δ ² H _{wax-T} ^{c,d} | -16 | 11 | 35 | 16 | -161 | 8 |
| Temperature | | | | | | |
| Chinese Loess Plateau MAAT ^a | -3 | 32 | 13 | 14 | 22 | 9 |
| Northern South China Sea U ^K ₃₇ ' SST ^{c,d} | -84 | 4 | -66 | 8 | -5 | 10 |
| Other Chinese Loess Plateau Records | | | | | | |
| Chinese Loess Plateau Mean Grain Sizea | 103 | 6 | 126 | 11 | 173 | 11 |
| Chinese Loess Plateau Magnetic Susceptibility ^a | -77 | 9 | -45 | 14 | -17 | 5 |
| Chinese Loess Plateau δ ¹³ C ^a | | | 23 | 15 | -45 | 18 |

Notes. Italic and bold font show coherence at 80% and 95% confidence intervals, respectively. No data shown indicates lack of coherence at the 80% confidence interval. Isotope records multiplied by -1 for phase analysis, such that phasing relates to isotope minima.

- ^a Analyzed for 8 to 360 kyr at 1 kyr time steps.
- b Wang et al., 2001, 2008.
- ^c Analyzed for 67 to 350 kyr at 1 kyr time steps.
- d Thomas et al. 2014a, 2014b.

and GS may also be influenced by variables other than 'monsoon strength' (e.g., both may be influenced by temperature, and MS may be influenced by GS-controlled variations in pedogenesis, Li et al., submitted for publication), we use these proxies as best estimates of orbital-scale variations in summer and winter monsoon strength, respectively (Maher, 2008; Sun et al., 2012). We choose to not include $\delta^{13}C_{\text{wax}}$ in our data-based model, since vegetation is directly influenced by temperature and moisture availability (Liu et al., 2005), and the inclusion of $\delta^{13}C_{\text{wax}}$ would therefore effectively include temperature and moisture availability twice in our model. We call the resulting linear regression a "data-based model" for Chinese Loess Plateau δ^2H_{wax} . The best-fit data-based model is as follows (Fig. 4):

$$\delta^{2}$$
H_{wax} = -1.52 × GS - 1.88 × MS + 0.26 × MAAT
r = 0.35, p < 0.0001

Despite the fact that the input data for the model are dominated by primary orbital periods (Fig. 3), the data-based model has almost no variance at primary orbital periods (Fig. 5). Instead, the data-based model spectrum has remarkable similarities to the Chinese Loess Plateau $\delta^2 H_{\text{wax}}$ spectrum, with dominant heterodyne peaks at 72 and 31 kyr (Fig. 5). Furthermore, Chinese Loess Plateau $\delta^2 H_{\text{wax}}$ and the data-based model are coherent and nearly in phase at the 72 and 31 kyr heterodynes, suggesting that the data-based model captures the heterodyne variability of interest in the Chinese Loess Plateau $\delta^2 H_{wax}$ record. The data-based model does not capture variability at the 23 and 17 kyr periods, which are minor peaks in the Chinese Loess Plateau $\delta^2 H_{wax}$ spectrum. The relatively weak linear fit (r = 0.35) between the data-based model and Chinese Loess Plateau $\delta^2 H_{wax}$ is not an accurate representation of the similarity of the orbital-scale variance in these records, as the linear fit includes variance at suborbital periods that mask variance at the heterodyne periods of interest.

The sign of the input variables to the data-based model are consistent with their influence on precipitation $\delta^2 H$, a further indication that the data-based model reflects real-world processes on orbital time scales. Warm temperatures cause precipitation to fall with higher $\delta^2 H$ values, consistent with the sign of MAAT in the data-based model. A strong winter monsoon (i.e., strong north-

westerly winds), as represented by large GS values, carries more of 2 H-depleted continental moisture to the Chinese Loess Plateau, consistent with the sign of GS in the data-based model. Finally, a strong summer monsoon, as represented by large MS values, carries more of 2 H-depleted moisture from the Bay of Bengal and the South China Sea, consistent with the sign of MS in the data-based model. Both a strong summer monsoon and a strong winter monsoon result in lower precipitation δ^2 H values at opposite phases, thereby reducing the amount of variance at the primary orbital periods.

The data-based model captures much of the orbital-scale variability in Chinese Loess Plateau $\delta^2 H_{\text{wax}}$. We therefore infer that the coefficients of the input variables reflect their relative influence on orbital-scale water isotope variability on the Chinese Loess Plateau. The winter and summer monsoon exert the greatest and near-equal influence on water isotopes in the data-based model. Temperature explains less than 10% of the variance in the data-based model, perhaps because GS and MS incorporate aspects of temperature variability.

The interaction of processes associated with the summer and winter monsoons at dominant orbital periods causes the heterodynes observed in both the Chinese Loess Plateau $\delta^2 H_{wax}$ and the data-based model to be more dominant than in individual GS and MS records. Our data-based model suggests that precipitation isotopes and hydroclimate on the Chinese Loess Plateau are influenced roughly equally by summer and winter monsoon dynamics. Summer monsoon dynamics cause changes in local summer rainfall δ^{18} O and δ^{2} H via changes in the isotopic composition of vapor along the ocean-to-continent transport path (Lee et al., 2012; LeGrande and Schmidt, 2009; Liu et al., 2014; Pausata et al., 2011). Winter monsoon dynamics are manifested primarily as changes in local winter rainfall $\delta^{18}{\rm O}$ and $\delta^{2}{\rm H}$ driven by large-scale changes in the transport path, and by changes in relative humidity and vegetation cover (Baker et al., 2015; Lee et al., 2012). The interaction of summer and winter monsoon dynamics results in a water isotope record with complex spectral characteristics, a concept that we apply to clarify interpretations of water isotope records throughout Asia.

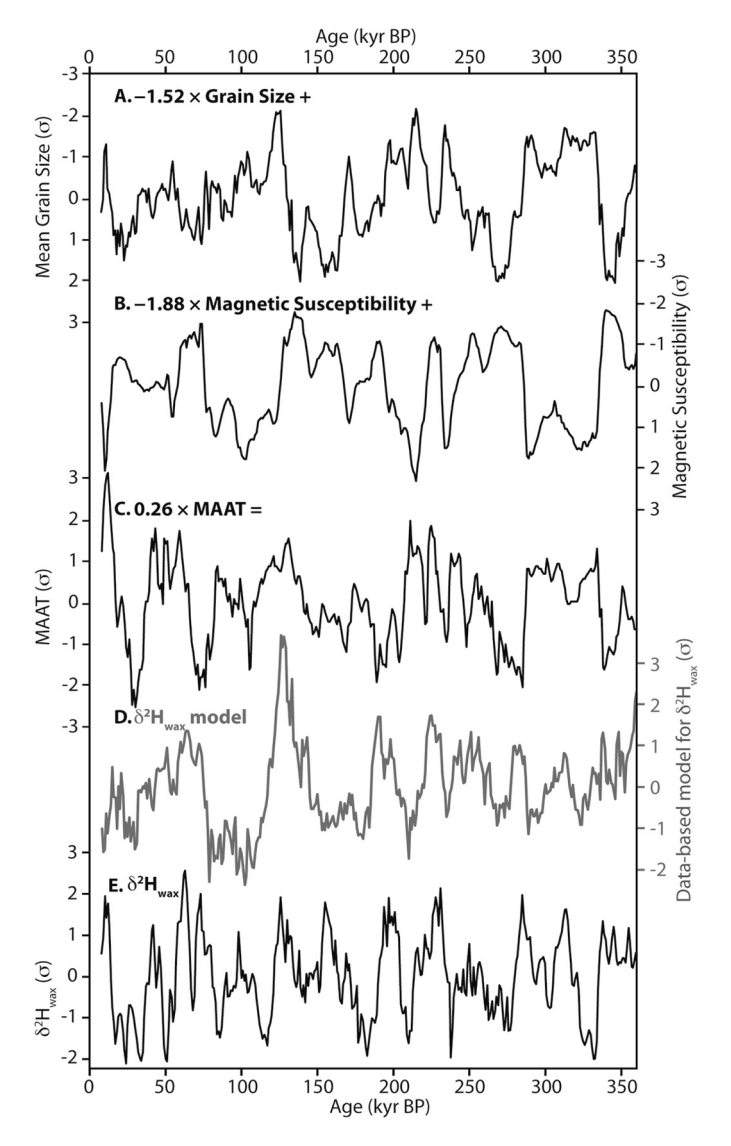


Fig. 4. Multiple linear regression model of Chinese Loess Plateau $\delta^2 H_{\text{wax}}$ using independent records of temperature, summer monsoon strength, and winter monsoon strength. A. Grain size at Weinan. B. Magnetic susceptibility at Weinan. C. brGDGT-inferred MAAT at Weinan. D. The "data-based model" time series resulting from the linear combination of GS, MS and MAAT, each multiplied by the coefficients shown in each panel. E. Chinese Loess Plateau $\delta^2 H_{\text{wax}}$. All records are plotted in the orientation that the model chose (e.g., negative grain size), which in all cases is consistent with known effects of the climate variables on precipitation $\delta^2 H$ (e.g., large grain size represents strong winter monsoons, which carry $^2 H$ -depleted precipitation to the Chinese Loess Plateau). All records normalized to zero average and standard deviation units.

5.2. Comparing variance among East Asian water isotope records to determine spatially varying summer- and winter-monsoon influence

Monsoons, as recorded by loess magnetic susceptibility, grain size, and other proxies are complex systems influenced by northern and southern hemisphere dynamics, as indicated by phasing at primary orbital periods (Clemens et al., 2010; Sun et al., 2015; Thomas et al., 2014a). Yet, the variance in the grain size and magnetic susceptibility records is concentrated at primary orbital periods (Fig. 3I, J), in contrast to the complex spectrum of the water isotope record on the Chinese Loess Plateau (Fig. 3B). Other water isotope records in East Asia also have complex spectra (Fig. 3C, D). It would be ideal to investigate the origin of these complex spectra as we did on the Chinese Loess Plateau, by combining independent records of winter and summer monsoon strength, temperature, and other variables reconstructed at the same locations, but such

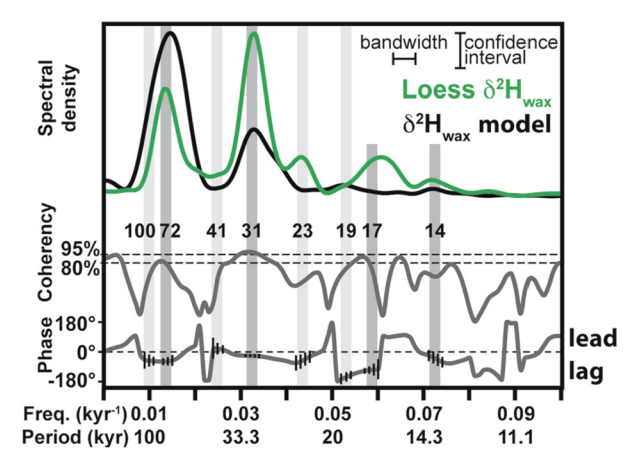


Fig. 5. Spectra of Chinese Loess Plateau $\delta^2 H_{\text{wax}}$, notch filtered to remove low-frequency variability (<0.005 kyr⁻¹) (green) and the data-based model for Chinese Loess Plateau $\delta^2 H_{\text{wax}}$ (black) during the past 360 kyr. Upper curves are spectral density, both on linear y-axes. The middle gray curve is coherency between the two records, 80 and 95% coherency levels are marked with dashed lines. The lower gray curve is the phase of $\delta^2 H_{\text{wax}}$ relative to the data-based model, uncertainty shown with black bars during periods of interest. A positive phase means $\delta^2 H_{\text{wax}}$ leads the data-based model, a negative phase means $\delta^2 H_{\text{wax}}$ lags the data-based model. Vertical bars highlight primary orbital periods (light gray) and heterodyne periods (dark gray), periodicity labeled with black numbering. (For interpretation of the references to color in this figure legend, the reader is referred to the web version of this article.)

complementary records do not exist at each site. We can, however, examine whether heterodyne periods are present in these other water isotope records. The presence of heterodynes would indicate the influence of multiple environmental variables interacting at different orbital periods.

5.2.1. Yangtze River Valley $\delta^{18}O_{cave}$ heterodynes

There are three key spectral characteristics in Yangtze River Valley $\delta^{18} O_{cave}$, which together indicate that non-linear interactions between multiple climate variables is occurring. These characteristics include:

- 1. A lower ratio of 23:19 kyr-band variance than in the local orbital forcing (23:19 kyr variance ratio of 12 in the local insolation forcing, ratio of 4 in Yangtze River Valley $\delta^{18}O_{cave}$).
- 2. Heterodynes that cannot be explained except by the interaction of primary periods.
- 3. An absence of variance at the 100 and 41 kyr bands.

Precession-band variance is dominant in Yangtze River Valley $\delta^{18}O_{cave}$: the 23 and 19 kyr periods compose 52% and 11% of total variance, respectively (Fig. 3C). If $\delta^{18}O_{cave}$ responds linearly to precession forcing, we would expect the ratio of 23 to 19 kyr variance to be consistent between the forcing and the proxy. The ratio of 23 to 19 kyr variance for summer, winter, and annual insolation forcing at 32°N, 0 to 360 kyr is 12:1 (i.e., the area of the 23 kyr peak is twelve times larger than the 19 kyr peak in the insolation forcing, independent of the season), whereas the ratio of 23 to 19 kyr variance in $\delta^{18}O_{cave}$ is 4:1. This suggests that some mechanism amplifies the 19 kyr periodicity relative to the 23 kyr periodicity in $\delta^{18}O_{cave}$. Interactions at primary orbital periods produces numerous heterodynes at periods close to 23 and 19 kyr (Table 1). More than 20% of these heterodynes are within 0.005 kyr⁻¹ of a precession frequency, meaning that the precession-scale variance in $\delta^{18}O_{cave}$ may, at least in part, be a result of heterodynederived variance. Xiaobailong and Bittoo $\delta^{18}O_{cave}$ both clearly contain large heterodyne variance (Fig. 3E, F; Section 5.2.3) supporting the possibility that the 23 and 19 kyr periods are at least partially heterodyne-derived.

Yangtze River Valley $\delta^{18} O_{cave}$ also contains small amounts of variance at 53 and 35 kyr, which are heterodyne periods (Fig. 3C, Table 1). The presence of these clear heterodyne periods provides additional evidence that multiple environmental variables operating at different orbital periods influence water isotopes in this system (Clemens et al., 2010).

Because Yangtze River Valley $\delta^{18}O_{cave}$ is clearly influenced by monsoon variability (Wang et al., 2008), which occurs at all three orbital periods (Fig. 3I, J), and $\delta^{18}O_{cave}$ responds strongly to precession-band variance, we would expect that Yangtze River Valley $\delta^{18}O_{cave}$ would exhibit at least some response to eccentricity and obliquity forcing. Yet, Yangtze River Valley $\delta^{18}O_{cave}$ contains almost no eccentricity or obliquity-band variance (100 and 41 kyr).

These three key spectral characteristics together indicate that Yangtze River Valley δ^{18} O_{cave} is influenced by the non-linear interaction of multiple environmental variables. Similar to the Chinese Loess Plateau, the environmental variables that influence Yangtze River Valley δ^{18} O_{cave} likely include summer and winter monsoons, but also include variables that are governed by different mechanisms, and therefore result in a different spectrum than observed for Chinese Loess Plateau δ^2 H_{wax}. These variables may include moisture from the East China Sea, locally recycled moisture, and/or karst hydrology dynamics (Baker et al., 2015; Duan et al., 2016; Lee et al., 2012; Sun and Wang, 2014).

5.2.2. Pearl River Valley $\delta^2 H_{wax}$ is dominated by primary orbital periods In contrast to Chinese Loess Plateau $\delta^2 H_{wax}$ and Yangtze River Valley $\delta^{18}O_{cave}$, the spectrum of Pearl River Valley $\delta^{2}H_{wax}$ is dominated by variance at all three primary orbital periods (Fig. 3D). The simpler spectrum of Pearl River Valley $\delta^2 H_{\text{wax}}$ suggests either that fewer environmental variables influence water isotopes in this region, or that one variable exerts a dominant influence. Today, oceanic moisture sources contribute a majority of precipitation to the Pearl River Valley (Sun and Wang, 2014). We demonstrated previously that precipitation isotopes in the Pearl River Valley respond directly to orbital forcing at the precession band (Thomas et al., 2014a). Water isotopes in this region also respond in phase with forcing at the eccentricity and obliquity bands. Even so, there are small heterodyne peaks at 55 and 28 kyr. The minor heterodyne peaks suggest that there is a minor influence of other environmental variables on Pearl River Valley $\delta^2 H_{wax}$, likely the winter monsoon (continental moisture sources) (Sun and Wang, 2014).

5.2.3. Northern India and Southern China $\delta^{18}O_{cave}$ contain heterodynes In addition to the three orbital-scale East Asian water isotope records, there are orbital-scale $\delta^{18}O_{cave}$ records from Xiaobailong Cave in southern China and Bittoo Cave in northern India (Figs. 1, A3) (Cai et al., 2015; Kathayat et al., 2016). The spectra of these records contain peaks both at primary and at heterodyne periods (Fig. 3E, F). The presence of heterodynes in these spectra is evidence that environmental variables in addition to summer monsoon precipitation influence $\delta^{18}O_{cave}$ at these sites. Xiaobailong Cave receives oceanic moisture from both the Bay of Bengal and from the South China Sea, in addition to continental moisture (Baker et al., 2015; Cai et al., 2015). Even Bittoo Cave, within the relatively simple Indian Monsoon region, receives moisture from multiple sources in the modern, including oceanic moisture from the Arabian Sea and the Bay of Bengal, and continental moisture from the northwest (Kathayat et al., 2016, Fig. S1). The large heterodyne peaks in the Xiaobailong and Bittoo cave records are evidence that, like in East Asia, multiple environmental variables influence precipitation isotopes at these sites. These findings bolster studies demonstrating that precipitation isotopes throughout Asia do not reflect local precipitation amount (Caley et al., 2014; Lee et al., 2012; LeGrande and Schmidt, 2009; Maher, 2008; Pausata et al., 2011; Thomas et al., 2014a, among others). These

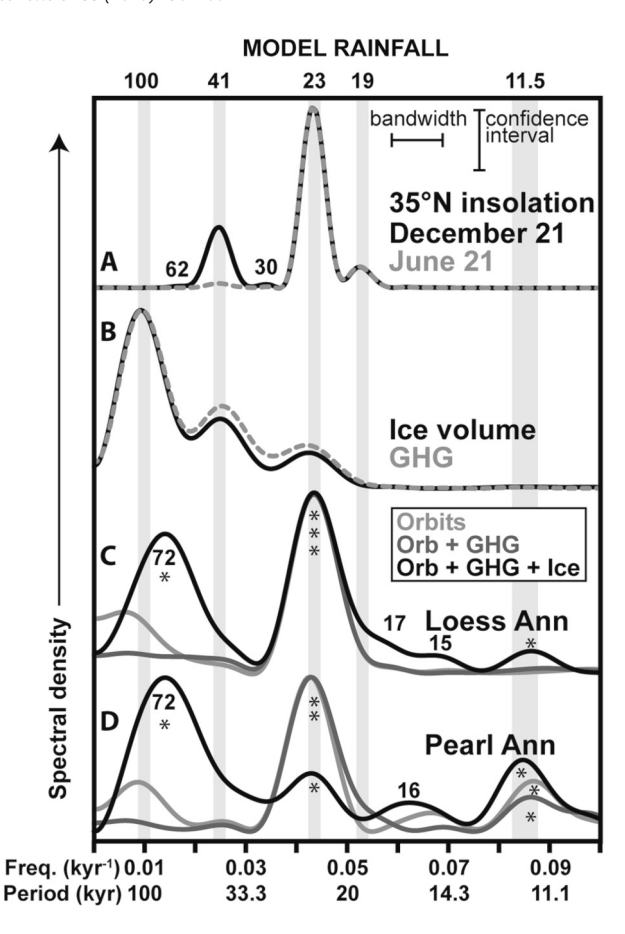


Fig. 6. Spectra of time series of annual precipitation amount in East Asia modeled using a 300 kyr fully coupled transient simulation of CCSM3 (Chen et al., 2011). All spectral analyses were completed for 0 to 300 ka. Vertical bars highlight primary orbital periods, labeled with black numbers at top. Heterodyne peaks in individual records are labeled with black numbers. Asterisks indicate peaks that exceed the 80% confidence bound in an f-test for periods shorter than 1/3 the length of each record (Paillard et al., 1996). A. December 21 (solid black) and June 21 (dashed gray) insolation at 35°N (Laskar et al., 2004). B. Ice volume (solid black) and greenhouse gas (GHG, dashed gray) forcing in the model. C. Annual precipitation amount in the four grid cells over the Chinese Loess Plateau in three sensitivity simulations: one with orbital changes only (light gray), one with orbital and GHG changes (dark gray), and one with orbital, GHG, and ice volume changes (black). D. Same as C. but for grid cells over the Pearl River Valley. Complex spectra, i.e., those that contain heterodynes, arise in the simulation that includes ice volume, indicating that glacial boundary conditions are important drivers of hydroclimate in East Asia.

finding also indicate that the spectral peaks of precipitation isotope records can help identify the environmental variables that influence precipitation isotopes at each site.

5.3. Rainfall in a fully coupled transient model simulation of East Asia

A 21-kyr isotope-enabled transient model simulation demonstrates that moisture transport and upstream rainout cause glacial-interglacial-scale precipitation isotope variability in East Asia (Liu et al., 2014). A 150-kyr isotope-enabled transient model simulation reveals that precipitation from multiple oceanic sources and multiple seasons influences precipitation isotopes throughout Asia (Caley et al., 2014). However, 21 or 150 kyr is not long enough to robustly examine the role of obliquity and the modulation of precession by eccentricity in modeled precipitation isotopes. Although longer isotope-enabled transient simulations do not yet exist, we can use an existing 300 kyr transient simulation to better understand the mechanisms that influence precipitation amount in East Asia (Fig. 6) (Chen et al., 2011).

Three 300-kyr-long experiments were run using three different sets of forcing: (1) Orbital variations only, (2) Orbital and

greenhouse gas variations; and (3) Orbital, greenhouse gas, and ice volume/sea level variations (Figs. 6A, 6B). We analyze time series of modeled annual precipitation amount over the Chinese Loess Plateau and the Pearl River catchment. The simulations without ice volume forcing contain simple spectra, with peaks concentrated at primary orbital periods and the greatest variance at the 23 kyr band (gray spectra, Figs. 6C, 6D). The simulation with ice volume forcing contains complex spectra, with peaks at the 72 kyr heterodyne as in Chinese Loess Plateau $\delta^2 H_{wax}$ (Fig. 3B) in addition to power at the 23 and 11.5 kyr (half precession) bands (black spectra, Figs. 6C, 6D). Water isotope proxy records indicate a northward increase in heterodyne variance (Fig. 3), which we interpret to indicate a northward increase in winter monsoon influence. The model shows the opposite trend, with greater heterodyne variance in southern China, indicating either that the model does not replicate the spatial variability observed in the data, or that the factors governing precipitation dynamics are different than those governing precipitation isotope dynamics. The important aspect of the model result, however, is the presence of heterodynes when the forcings are more complex, which suggests that model precipitation amount is the result of nonlinear interactions among processes operating at different orbital periods. These results highlight the influence that obliquity forcing and glacial boundary conditions have on East Asian monsoons, even in low-latitude regions (Bosmans et al., 2015; Chen et al., 2011), and underscore the importance of interpreting precipitation isotope records in the context of the multiple environmental variables that influence precipitation isotopes.

6. Summary

The existence of heterodynes in all orbital-scale water isotope records in the Asian monsoon region (Fig. 3B-F) is evidence that water isotopes are strongly influenced by multiple climate variables. Heterodynes can only be produced when variables operating at different orbital periods interact. Records of temperature, summer-monsoon strength, and winter-monsoon strength have simple spectra that lack major heterodyne peaks (Fig. 3 H-K), providing further evidence that water isotopes do not respond solely to the summer or winter monsoon or to any other single environmental variable. Rather, water isotopes in Asia are likely influenced by multiple environmental variables, including both continental and oceanic moisture sources, terrestrial precipitation recycling, and temperature. The spectra of water isotope proxy records in East Asia increase in complexity from south to north, indicating increasing influence of multiple environmental parameters. The combination of independent temperature, summer monsoon, and winter monsoon records from the Chinese Loess Plateau demonstrates that precipitation isotopes in this region are influenced equally by summer (oceanic) and winter (continental) monsoon variability. The influence of the winter monsoon (continental moisture) decreases southward, until it plays only a minor role in the Pearl River Valley (Thomas et al., 2014a).

Consideration of both summer and winter monsoon dynamics is key to fully exploiting the information contained in water isotope records in East Asia. Precipitation in a long transient climate model simulation contains complex spectra when run with full glacial boundary conditions, indicating that hydroclimate in East Asia is impacted both by internal and external forcing mechanisms. Water isotope records, in concert with fully coupled transient isotope-enabled climate models, will help us to decipher the mechanisms that cause changes in oceanic and continental moisture sources, and in turn to influence precipitation variability in Asia.

Acknowledgements

This research was supported by an NSF Graduate Research Fellowship to EKT, NSF AGS-1002504 and OCE-1129408 to SCC, an International Innovation Partnership Program from the Chinese Academy of Sciences (KZZD-EW-TZ-03) to YS, NSF 1129316 to GC, and NSF 41130105 to ZL. EKT is currently an NSF EAR Postdoctoral Fellow, NSF 1349595. We thank Rafael Tarozo, Julia Guimond, Audrey Lew, John Ryan-Henry, and Pamela Wegener for lab support. Sampling of the Weinan loess section was supported by IEE-CAS. Weinan and Lantian chronological and geochemical data are freely available at the NOAA/World Data Center for Paleoclimatology (https://ncdc.noaa.gov/paleo/). We thank Thibaut Caley and two anonymous reviewers for their comments.

Appendix A. Supplementary material

Supplementary material related to this article can be found online at http://dx.doi.org/10.1016/j.epsl.2016.09.044.

References

- Baker, A.J., Sodemann, H., Baldini, J.U.L., Breitenbach, S.F.M., Johnson, K.R., van Hunen, J., Zhang, P., 2015. Seasonality of westerly moisture transport in the East Asian summer monsoon and its implications for interpreting precipitation δ^{18} O. J. Geophys. Res., Atmos. 120. http://dx.doi.org/10.1002/2014JD022919.
- Bosmans, J.H.C., Hilgen, F.J., Tuenter, E., Lourens, L.J., 2015. Obliquity forcing of low-latitude climate. Clim. Past 11, 1335–1346. http://dx.doi.org/10.5194/cp-11-1335-2015
- Bradley, C., Baker, A., Jex, C.N., Leng, M.J., 2010. Hydrological uncertainties in the modelling of cave drip-water δ^{18} O and the implications for stalagmite palaeoclimate reconstructions. Quat. Sci. Rev. 29, 2201–2214.
- Caballero-Gill, R.P., Clemens, S.C., Prell, W.L., 2012. Direct correlation of Chinese speleothem $\delta^{18}O$ and South China Sea planktonic $\delta^{18}O$: transferring a speleothem chronology to the benthic marine chronology. Paleoceanography 27, PA2203. http://dx.doi.org/10.1029/2011PA002268.
- Cai, Y., Fung, I.Y., Edwards, R.L., An, Z., Cheng, H., Lee, J.-E., Tan, L., Shen, C.-C., Wang, X., Day, J.A., Zhou, W., Kelly, M.J., Chiang, J.C.H., 2015. Variability of stalagmite-inferred Indian monsoon precipitation over the past 252,000 y. PNAS 112, 2954–2959. http://dx.doi.org/10.1029/2011PA002268.
- Caley, T., Roche, D.M., Renssen, H., 2014. Orbital Asian summer monsoon dynamics revealed using an isotope-enabled global climate model. Nat. Commun. 5. http://dx.doi.org/10.1038/ncomms6371.
- Chen, G.-S., Liu, Z., Clemens, S.C., Prell, W.L., Liu, X., 2011. Modeling the time-dependent response of the Asian summer monsoon to obliquity forcing in a coupled GCM: a PHASEMAP sensitivity experiment. Clim. Dyn. 36, 695–710. http://dx.doi.org/10.1007/s00382-010-0740-3.
- Chen, X., Hu, B., Yu, R., 2005. Spatial and temporal variation of phenological growing season and climate change impacts in temperate eastern China. Glob. Change Biol. 11, 1118–1130. http://dx.doi.org/10.1111/j.1365-2486.2005.00974.x.
- Cheng, H., Edwards, R.L., Broecker, W.S., Denton, G.H., Kong, X., Wang, Y., Zhang, R., Wang, X., 2009. Ice age terminations. Science 326, 248–252. http://dx.doi.org/ 10.1126/science.1177840.
- Cheng, H., Edwards, R.L., Sinha, A., Spötl, C., Yi, L., Chen, S., Kelly, M., Kathayat, G., Wang, X., Li, X., Kong, X., Wang, Y., Ning, Y., Zhang, H., 2016. The Asian monsoon over the past 640,000 years and ice age terminations. Nature 534, 640–646. http://dx.doi.org/10.1038/nature18591.
- Chiang, J.C.H., Fung, I.Y., Wu, C.-H., Cai, Y., Edman, J.P., Liu, Y., Day, J.A., Bhattacharya, T., Mondal, Y., Labrousse, C.A., 2015. Role of seasonal transitions and westerly jets in East Asian paleoclimate. Quat. Sci. Rev. 108, 111–129. http://dx.doi.org/10.1016/j.quascirev.2014.11.009.
- Clemens, S.C., Prell, W.L., Sun, Y., 2010. Orbital-scale timing and mechanisms driving Late Pleistocene Indo-Asian summer monsoons: reinterpreting cave speleothem δ¹⁸O. Paleoceanography 25. http://dx.doi.org/10.1029/2010PA001926.
- Duan, W., Ruan, J., Luo, W., Li, T., Tian, L., Zeng, G., Zhang, D., Bai, Y., Li, J., Tao, T., Zhang, P., Baker, A., Tan, M., 2016. The transfer of seasonal isotopic variability between precipitation and drip water at eight caves in the monsoon regions of China. Geochim. Cosmochim. Acta 183, 250–266. http://dx.doi.org/10.1016/j.gca.2016.03.037.
- Gao, L., Nie, J., Clemens, S., Liu, W., Sun, J., Zech, R., Huang, Y., 2012a. The importance of solar insolation on the temperature variations for the past 110 kyr on the Chinese Loess Plateau. Palaeogeogr. Palaeoclimatol. Palaeoecol. 317–318, 128–133. http://dx.doi.org/10.1016/j.palaeo.2011.12.021.
- Gao, L., Tsai, Y.-J., Huang, Y., 2012b. Assessing the rate and timing of leaf wax regeneration in *Fraxinus americana* using stable hydrogen isotope labeling. Rapid Commun. Mass Spectrom. 26, 2241–2250. http://dx.doi.org/10.1002/rcm.6348.

- Hao, Q., Wang, L., Oldfield, F., Peng, S., Qin, L., Song, Y., Xu, B., Qiao, Y., Bloemendal, J., Guo, Z., 2012. Delayed build-up of Arctic ice sheets during 400,000-year minima in insolation variability. Nature 490, 393–396. http://dx.doi.org/10.1038/nature11493.
- Howell, P., Pisias, N., Ballance, J., Baughman, J., Ochs, L., 2006. ARAND Time-Series Analysis Software. Brown University, Providence, RI.
- Huguet, C., Hopmans, E.C., Febo-Ayala, W., Thompson, D.H., Sinninghe Damsté, J.S., Schouten, S., 2006. An improved method to determine the absolute abundance of glycerol dibiphytanyl glycerol tetraether lipids. Org. Geochem. 37, 1036–1041. http://dx.doi.org/10.1016/j.orggeochem.2006.05.008.
- IAEA/WMO, 2011. Global Network of Isotopes in Precipitation. The GNIP Database. Johnson, K.R., Ingram, B.L., 2004. Spatial and temporal variability in the stable isotope systematics of modern precipitation in China: implications for paleoclimate reconstructions. Earth Planet. Sci. Lett. 220, 365–377. http://dx.doi.org/10.1016/S0012-821X(04)00036-6.
- Kahmen, A., Hoffmann, B., Schefuß, E., Arndt, S.K., Cernusak, L.A., West, J.B., Sachse, D., 2013. Leaf water deuterium enrichment shapes leaf wax n-alkane δD values of angiosperm plants II: observational evidence and global implications. Geochim. Cosmochim. Acta 111, 50–63. http://dx.doi.org/10.1016/j.gca. 2012.09.004
- Kathayat, G., Cheng, H., Sinha, A., Spötl, C., Edwards, R.L., Zhang, H., Li, X., Yi, L., Ning, Y., Cai, Y., Lui, W.L., Breitenbach, S.F.M., 2016. Indian monsoon variability on millennial-orbital timescales. Sci. Rep. 6, 24374. http://dx.doi.org/10.1038/ srep24374.
- Laskar, J., Robutel, P., Joutel, F., Gastineau, M., Correia, A.C.M., Levrard, B., 2004. A long-term numerical solution for the insolation quantities of the Earth. Astron. Astrophys. 428, 261–285. http://dx.doi.org/10.1051/0004-6361:20041335.
- Lee, J.-E., Risi, C., Fung, I., Worden, J., Scheepmaker, R.A., Lintner, B., Frankenberg, C., 2012. Asian monsoon hydrometeorology from TES and SCIAMACHY water vapor isotope measurements and LMDZ simulations: implications for speleothem climate record interpretation. J. Geophys. Res. 117, D15112. http://dx.doi.org/ 10.1029/2011ID017133.
- LeGrande, A.N., Schmidt, G.A., 2009. Sources of Holocene variability of oxygen isotopes in paleoclimate archives. Clim. Past 5, 441–455. http://dx.doi.org/10.5194/cp-5-441-2009.
- Li, T., Liu, F., Abels, H.A., You, C.-F., Zhang, Z., Chen, J., Ji, J., Li, L., Li, L., Liu, H.-C., Ren, C., Xia, R., Zhao, L., Zhang, W., Li G., submitted for publication. Continued obliquity pacing of East Asian summer precipitation after the mid-Pleistocene transition. Earth Planet. Sci. Lett. http://dx.doi.org/10.1016/j.epsl.2016.09.045.
- Liu, W., Huang, Y., 2005. Compound specific D/H ratios and molecular distributions of higher plant leaf waxes as novel paleoenvironmental indicators in the Chinese Loess Plateau. Org. Geochem. 36, 851–860. http://dx.doi.org/10.1016/i.orggeochem.2005.01.006.
- Liu, W., Huang, Y., An, Z., Clemens, S.C., Li, L., Prell, W.L., Ning, Y., 2005. Summer monsoon intensity controls C4/C3 plant abundance during the last 35 ka in the Chinese Loess Plateau: carbon isotope evidence from bulk organic matter and individual leaf waxes. Palaeogeogr. Palaeoclimatol. Palaeoecol. 220, 243–254. http://dx.doi.org/10.1016/j.palaeo.2005.01.001.
- Liu, Z., Wen, X., Brady, E.C., Otto-Bliesner, B., Yu, G., Lu, H., Cheng, H., Wang, Y., Zheng, W., Ding, Y., Edwards, R.L., Cheng, J., Liu, W., Yang, H., 2014. Chinese cave records and the East Asia summer monsoon. Quat. Sci. Rev. 83, 115–128. http://dx.doi.org/10.1016/j.guascirev.2013.10.021.
- Loomis, S.E., Russell, J.M., Ladd, B., Street-Perrott, F.A., Sinninghe Damsté, J.S., 2012. Calibration and application of the branched GDGT temperature proxy on East African lake sediments. Earth Planet. Sci. Lett. 357–358, 277–288. http://dx.doi.org/10.1016/j.epsl.2012.09.031.
- Lorenz, S.J., Lohmann, G., 2004. Acceleration technique for Milankovitch type forcing in a coupled atmosphere-ocean circulation model: method and application for the Holocene. Clim. Dyn. 23, 727-743. http://dx.doi.org/10.1007/s00382-004-0469-v.
- Maher, B.A., 2008. Holocene variability of the East Asian summer monsoon from Chinese cave records: a re-assessment. Holocene 18, 861–866.
- NCDC NOAA, 2012. Global historical climatology network.

- Orland, I.J., Edwards, R.L., Cheng, H., Kozdon, R., Cross, M., Valley, J.W., 2015. Direct measurements of deglacial monsoon strength in a Chinese stalagmite. Geology 43, 555–558. http://dx.doi.org/10.1130/G36612.1.
- Paillard, D., Labeyrie, L., Yiou, P., 1996. Macintosh Program performs time-series analysis. Eos Trans. AGU 77. 379. http://dx.doi.org/10.1029/96E000259.
- Pausata, F.S.R., Battisti, D.S., Nisancioglu, K.H., Bitz, C.M., 2011. Chinese stalagmite δ^{18} O controlled by changes in the Indian monsoon during a simulated Heinrich event. Nat. Geosci. 4, 474–480. http://dx.doi.org/10.1038/ngeo1169.
- Peterse, F., Martínez-García, A., Zhou, B., Beets, C.J., Prins, M.A., Zheng, H., Eglinton, T.I., 2014. Molecular records of continental air temperature and monsoon precipitation variability in East Asia spanning the past 130,000 years. Quat. Sci. Rev. 83, 76–82. http://dx.doi.org/10.1016/j.quascirev.2013.11.001.
- Porter, S.C., An, Z., 1995. Correlation between climate events in the North Atlantic and China during the last glaciation. Nature 375, 305–308. http://dx.doi.org/ 10.1038/375305a0.
- Rao, Z., Zhu, Z., Jia, G., Henderson, A.C.G., Xue, Q., Wang, S., 2009. Compound specific δD values of long chain n-alkanes derived from terrestrial higher plants are indicative of the δD of meteoric waters: evidence from surface soils in eastern China. Org. Geochem. 40, 922–930. http://dx.doi.org/10.1016/j.orggeochem. 2009.04.011.
- Rial, J.A., Anaclerio, C.A., 2000. Understanding nonlinear responses of the climate system to orbital forcing. Quat. Sci. Rev. 19, 1709–1722.
- Sun, B., Wang, H., 2014. Analysis of the major atmospheric moisture sources affecting three sub-regions of East China. Int. J. Climatol. 35, 2243–2257. http://dx.doi.org/10.1002/joc.4145.
- Sun, D., Shaw, J., An, Z., Cheng, M., Yue, L., 1998. Magnetostratigraphy and paleoclimatic interpretation of a continuous 7.2 Ma Late Cenozoic Eolian sediments from the Chinese Loess Plateau. Geophys. Res. Lett. 25, 85–88. http://dx.doi.org/ 10.1029/97G103353.
- Sun, Y., An, Z., Clemens, S.C., Bloemendal, J., Vandenberghe, J., 2010. Seven million years of wind and precipitation variability on the Chinese Loess Plateau. Earth Planet. Sci. Lett. 297, 525–535. http://dx.doi.org/10.1016/j.epsl.2010.07.004.
- Sun, Y., Clemens, S.C., An, Z., Yu, Z., 2006. Astronomical timescale and palaeoclimatic implication of stacked 3.6-Myr monsoon records from the Chinese Loess Plateau. Ouat. Sci. Rev. 25. 33–48.
- Sun, Y., Clemens, S.C., Morrill, C., Lin, X., Wang, X., An, Z., 2012. Influence of Atlantic meridional overturning circulation on the East Asian winter monsoon. Nat. Geosci. 5, 46–49. http://dx.doi.org/10.1038/ngeo1326.
- Sun, Y., Kutzbach, J., An, Z., Clemens, S., Liu, Z., Liu, W., Liu, X., Shi, Z., Zheng, W., Liang, L., Yan, Y., Li, Y., 2015. Astronomical and glacial forcing of East Asian summer monsoon variability. Quat. Sci. Rev. 115, 132–142. http://dx.doi.org/10.1016/ j.quascirev.2015.03.009.
- Thomas, E.K., Clemens, S.C., Prell, W.L., Herbert, T.D., Huang, Y., Liu, Z., Damsté, J.S.S., Sun, Y., Wen, X., 2014a. Temperature and leaf wax δ^2 H records demonstrate seasonal and regional controls on Asian monsoon proxies. Geology 42, 1075–1078. http://dx.doi.org/10.1130/G36289.1.
- Thomas, E.K., Huang, Y., Morrill, C., Zhao, J., Wegener, P., Clemens, S.C., Colman, S.M., Gao, L., 2014b. Abundant C₄ plants on the Tibetan Plateau during the Lateglacial and early Holocene. Quat. Sci. Rev. 87, 24–33. http://dx.doi.org/10.1016/j.quascirev.2013.12.014.
- Thomas, E.K., Huang, Y., Clemens, S.C., Colman, S.M., Morrill, C., Wegener, P., Zhao, J., 2016. Changes in dominant moisture sources and the consequences for hydroclimate on the northeastern Tibetan Plateau during the past 32 kyr. Quat. Sci. Rev., Part A 131, 157–167. http://dx.doi.org/10.1016/j.quascirev.2015.11.003.
- Wang, Y., Cheng, H., Edwards, R.L., Kong, X., Shao, X., Chen, S., Wu, J., Jiang, X., Wang, X., An, Z., 2008. Millennial- and orbital-scale changes in the East Asian monsoon over the past 224,000 years. Nature 451, 1090–1093. http://dx.doi.org/10.1038/nature06692.
- Yang, H., Pancost, R.D., Dang, X., Zhou, X., Evershed, R.P., Xiao, G., Tang, C., Gao, L., Guo, Z., Xie, S., 2014. Correlations between microbial tetraether lipids and environmental variables in Chinese soils: optimizing the paleoreconstructions in semi-arid and arid regions. Geochim. Cosmochim. Acta 126, 49–69. http://dx.doi.org/10.1016/j.gca.2013.10.041.